Critical point fluctuations in supported lipid membranes

Simon D. Connell,*[a] George Heath,[a] Peter D. Olmsted[a] and Anastasia Kisil[b]

Received 10th July 2012, Accepted 23rd July 2012
DOI: 10.1039/c2fd20119d

In this paper, we demonstrate that it is possible to observe many aspects of critical phenomena in supported lipid bilayers using atomic force microscopy (AFM) with the aid of stable and precise temperature control. The regions of criticality were determined by accurately measuring and calculating phase diagrams for the 2 phase L_d–L_o region, and tracking how it moves with temperature, then increasing the sampling density around the estimated critical regions. Compositional fluctuations were observed above the critical temperature (T_c) and characterised using a spatial correlation function. From this analysis, the phase transition was found to be most closely described by the 2D Ising model, showing it is a critical transition. Below T_c roughening of the domain boundaries occurred due to the reduction in line tension close to the critical point. Smaller scale density fluctuations were also detected just below T_c. At T_c, we believe we have observed fluctuations on length scales greater than 10 μm. The region of critically fluctuating 10–100 nm nanodomains has been found to extend a considerable distance above T_c to temperatures within the biological range, and seem to be an ideal candidate for the actual structure of lipid rafts in cell membranes. Although evidence for this idea has recently emerged, this is the first direct evidence for nanoscale domains in the critical region.

Introduction

What governs the size and shape of the domains we observe in phase separating lipid biomembranes? A good description of the unanswered questions surrounding the phase separation of biological membranes has recently been presented by Feigenson.[1] Much research has gone into the study of lipid domains, mainly using techniques such as NMR[2] or neutron scattering of multiple ordered layers,[3] fluorescence microscopy of giant unilamellar vesicles (GUVs)[4] and FRET.[5] These techniques work on different length scales, and there are often discrepancies between them that must be resolved. For instance, for certain types of lipid mixture (the so called type I mixtures described by Feigenson[1]), the GUVs appear to be in a continuous single phase where one would expect phase separation to occur according to the established phase diagrams. FRET measurements, limited to distances of up to 50 nm, seem to indicate that there are indeed separate co-existing phases, so the domains must be much smaller than the resolution limit of optical microscopy (approximately 300 nm). AFM can cover this length scale, ranging from 10's of microns down to the nanometre level. It is also capable of imaging domain

[a]*School of Physics and Astronomy, University of Leeds, Leeds, UK. E-mail: s.d.a.connell@leeds.ac.uk; Tel: +00 44 113 3438241*
[b]*Centre for Mathematical Sciences, University of Cambridge, UK*

dynamics, such as the growth of domains as a single phase is cooled into a region of phase coexistence.[6,7]

We want to know the compositionally dependent shape and size of domains present (if any), on a nanometre or micron scale; are they discrete domains or a continuous network (nucleated or spinodal); are they stable or transient? Once all these questions have been answered, then we can begin to understand how membrane proteins interact with and partition into the various phases, and how model membranes relate to the properties of more complex and compositionally heterogeneous biological cell membranes.

In this paper, we will only focus on the lipid membrane, and not on its interactions with proteins (although this is a direction we are currently pursuing). We will also only concentrate on the high cholesterol two-phase coexistence region, which separates into two liquid phases, termed the liquid ordered (L_o) and liquid disordered (L_d, equivalent to the L_α phase). Animal cell plasma membranes have 30–45 mol% cholesterol, which is towards the upper end of this two-phase region in model membranes, perhaps extending out into the single L_o phase. This then seems to be the region of the phase diagram of most relevance to biological systems, and will be the focus of this study.

Evidence is growing to show that some native biomembranes may tune their compositions to be near a critical point at a given temperature in order to exploit the delicate balance between phases.[8] A small change in composition (and hence a small amount of energy expended for the cell) can radically alter its chemical and mechanical properties. This idea is not new,[9] but experimental evidence has only begun to emerge in recent years.[10–12] It has been proposed that critical fluctuations in both model and plasma membranes are what define lipid rafts. Out-of-equilibrium processes might govern domain sizes rather than the equilibrium structures, so perhaps the actual domain structures observed are not at equilibrium, and are not relevant.[13] The size and dynamics of domains in cell membranes is not explained by the simple equilibrium models: they could be kinetically trapped, or under continuous lipid turnover.

If the existence of nanodomains is likely around a critical point in the phase diagram, then what are their sizes, and how large is the critical region? In this work, we aim to characterise this critical behaviour. As the L_o phase is a laterally condensed phase, it has a lower area per molecule and a correspondingly thicker bilayer, by up to 0.8 nm. This difference is the signal measured by atomic force microscopy used in this work. At the boundary, there will be a mismatch between the hydrophobic regions leading to a line tension. As the two phases get closer together in composition (*i.e.*, near a critical point), the hydrophobic mismatch reduces and the line tension falls.[14] Line tension acts to minimise the phase boundary length, and is the driving force behind the coalescence of small domains into larger domains, minimising the perimeter length and, therefore, the interfacial energy. However, if the line tension is small enough, then this could be balanced by the entropy gained by having many small domains. It might, therefore, be expected that small nanodomains will be more stable at compositions close to a critical point. How relevant are these studies of model membranes to real cell membrane?

Although it has been unequivocally established that plasma membranes undergo phase separation,[15] it is nonetheless a fact that the lipid composition of cell membranes is more complex than three synthetic molecules with a wide distribution of chain length and headgroup chemistry. Lipid molecules that are somewhere between the properties of the ideal unsaturated lipid and saturated lipid will likely segregate near the phase boundaries, reducing the hydrophobic mismatch and reducing line tension. Mixed chain lipids, such as POPC, which possess a saturated and unsaturated chain, are also thought to segregate near a phase boundary, and studies into the effects of these so-called "edge-actant" or "line-actant" molecules has recently attracted some attention.[16] Reduced line tension will act to stabilize domains of a small size, reducing the driving force for Ostwald ripening.

Materials and methods

Supported bilayer formation

Supported lipid bilayers were formed using the vesicle rupture method.[17] Briefly, the stock solutions of each lipid component (at 5 mM in chloroform, supplied by Avanti either dry or in a sealed vial dissolved in chloroform) were mixed in a small vial to the correct molar proportion. The chloroform was removed first by drying under a gentle stream of N_2 and then for at least a couple of hours under vacuum, before being hydrated with water to a final lipid concentration of 1 mg ml^{-1} and vortexed to produce a milky white solution of multi-lamellar vesicles. This suspension was tip-sonicated until clear, usually for around 10 min, indicating the formation of small unilamellar vesicles (SUVs). 50 μL of this solution was introduced to a freshly cleaved mica substrate and incubated in a sealed humid chamber within an oven at 45–50 °C for 20 min. This elevated temperature is particularly important when preparing mixtures that phase separate into solid and liquid domains. Seantier *et al.*[18] clearly established that there were differences in the progress of supported bilayer formation depending on whether the temperature was above or below the main transition temperature of the lipid molecules. In this case, we are concentrating on a region of separation into two liquid phases, L_d and L_o, but even so, there are clear material and chemical differences between these two phases that are eliminated by increasing the temperature such that deposition occurs when the lipids are in a single homogenous liquid phase. By this method, we can be certain that the bilayer composition on the surface is the same as the bulk composition, born out by the similarity in the final determined phase diagram. Elevated temperatures and longer incubation times result in clean defect-free bilayers. The final step is a rinse across the top of the bilayer to remove the remaining unruptured vesicles still weakly attached to the substrate, together with suspended vesicles. Rinsing is performed approximately 10 times with 200 μL fairly vigorous jets from a Gilson pipette, the wash directed parallel across the top surface of the bilayer. The hydrated bilayer is then carefully inserted into the AFM taking care that it doesn't dry out or that the liquid drop doesn't fall off, which would result in the delicate bilayer being ripped off.

Atomic force microscopy

AFM experiments at room temperature (22 °C) and above were performed using a Bruker Multimode AFM on a Nanoscope IV controller. Bruker NP probes were used, the shorter 0.12 N m^{-1} probe in preference. Although tapping mode in liquids at frequencies of 8–10 kHz can result in sharper looking images, more stable imaging over time and is less prone to thermal drift effects, in this study contact mode was used. Due to the difference in the visco-elastic properties between the two lipid phases, the amplitude-tip separation response was different (visible in the different tapping phase contrasts between domains). This additional signal leads to quantitative differences between the bilayer heights measured with contact mode and tapping mode in a non-trivial manner. In this study, we used the height difference between the L_d and L_o phases as a proxy for the order parameter, so we must be confident this measurement is correct. Contact mode eliminates the complexity in the interpretation, and a low force of <0.2 nN was used for direct comparability. Although the different material properties between the phases is also evident in contact mode (the softer L_d phase can be more compressible), this complexity is well understood (for example see Das *et al.*[19]). This is also the reason we do not use sharpened probes (for example, Bruker NP-S) for a more controllable tip–bilayer interaction at higher forces. The sharpened tips have a tendency to penetrate the bilayer at a relatively low applied force of around 1 nN.

Temperature control

Temperature control was achieved on the Multimode AFM using a feedback controlled Bruker heater stage. The internal thermocouple in the heater cap was disconnected, and the feedback controller was connected to a very fine thermocouple inserted in the AFM fluid cell and rested on the mica surface about 2 mm to one side of the probe, immersed in the liquid. By this method, we have exact control of the temperature of the bilayer, removing the problem of thermal gradients from the heater element, *via* the metal stub, epoxy glue layer and mica substrate. When temperature control below <25 °C was required, a Bruker Bioscope AFM head was used, which was mounted on a home-built heater–cooler stage. This incorporates the workings of a Linkam optical microcope heater–cooler stage, with the sample mounted directly on a silver block containing a resistive heater element and pipes to carry liquid nitrogen, which was pumped continuously around. Although noise levels from the pump were just about acceptable whilst imaging gel phase domains with heights above the L_d phase of 1.0–1.4 nm (in other experiments), the height difference in these critical mixtures is regularly <0.4 nm, which was virtually obscured by the pump noise. A custom bungy-mass anti-vibration platform was built to isolate the noise, which was attenuated to a level where critical domains were visible. Temperature stability was <0.1 °C, with a maximum possible ramp rate of 10 °C s^{-1}, allowing for immediate quenching from a single phase to regions of phase separation if required. Images were not continuously acquired during the temperature ramps due to the thermal bending of gold coated AFM cantilevers *via* the bimetallic effect, and hence large drifts in the imaging force. Control of the imaging force was important in this study to reproducibly measure the difference in height between domains which have differing compressibility modulii. Rather, the temperature was incremented in 0.5 °C steps and left to equilibrate for approximately 20 s until the cantilever drift subsided before approaching the probe and imaging the features.

Image processing

Automated domain area and autocorrelation function measurements require binary images. The conversion of an AFM generated 3D surface of the domains should be straightforward, achieved by setting the threshold level equidistant between the L_o and L_d z-levels. Unfortunately, AFM images of very flat samples (z-features of several nm in height over micron length scans) contain instrumental artefacts relating to the scanning geometry, resulting in a sometimes complex distortion or image warp on the same scale as the image features. Images must therefore be carefully levelled to ensure a clean threshold can be set to discriminate the two phases. The standard third order polynomial line fit was often insufficient, particularly when the difference in domain heights was below 0.5 nm. Depending on the severity of non-linear image distortion encountered, one of two methods was used. The first simple procedure was a background subtraction in NIH Image J using a user definable rolling ball (usually >50 pixels). The second method used on more problematic backgrounds involved performing repeated Gaussian smoothing in x and y (separately), choosing an appropriate smoothing distance such that all domain features were obliterated, whilst retaining the background distortion. This background image was then arithmetically subtracted from the original. As the background curvature was usually in the x direction following the initial polynomial line levelling, the chosen y-smoothing would be much stronger than the x-smoothing.

Determination of phase diagrams

A procedure similar to that of Veatch *et al.*[4] and Juhasz *et al.*[20] was developed for use with AFM images, using the measured domain areas together with the lever rule. In

a phase separated system of two species A and B, lipid A is apportioned between the two phases according to:

$$\bar{c} = \alpha c_1 + (1 - \alpha)c_2, \tag{1}$$

where $\bar{c}$ is the average mole fraction of lipid A in the system (*i.e.*, the starting composition), α is the mole fraction of phase 1 in the system, and c_1 and c_2 are the mole fractions of lipid A in phases 1 and 2. The relative deviations of the phase 1 and 2 compositions from the mean composition are thus given by the lever rule:

$$\frac{c_1 - \bar{c}}{\bar{c} - c_2} = \frac{1 - \alpha}{\alpha}. \tag{2}$$

That is, the ratio of the molar fractions of material in the two phases is equal to the ratio of the distances along the tie lines from the average lipid composition to the boundaries of the two-phase region. In a ternary mixture there are actually two equations: one for $\bar{c}_A$ and one for $\bar{c}_B$, for example. However, the observed *area* fraction of phase 1 in the AFM images α' is not the *molar* fraction α, which must be calculated by considering the average surface area per lipid. Thus α is related to the observed area fraction of phase 1 by:

$$\alpha = \frac{\alpha'}{\alpha' + (1 - \alpha')\dfrac{a_1}{a_2}}, \tag{3}$$

where a_1 and a_2 are the average area per molecule (averaged over all species) in phases 1 and 2.

In certain instances, where more than one starting composition lie along the same tie line (*e.g.*, any binary system), we can express the tie line ratio as an equation for each composition, and then solve the simultaneous equations to determine the exact boundary location. If we substitute eqn (3) into eqn (1) we find a useful form:

$$\bar{c} = \frac{\alpha'}{\alpha' + (1 - \alpha')r_{12}}c_1 + \frac{(1 - \alpha')r_{12}}{\alpha' + (1 - \alpha')r_{12}}c_2, \tag{4}$$

where $r_{12} = a_1/a_2$.

The difficulty in carrying out this analysis for the ternary system studied here is that Chol tends to straighten the acyl chains hence reducing the molecular area, *i.e.*, a_1 and a_2 are Chol dependent. The area per molecule of DOPC and SM in lipid bilayers in the presence of Chol over a wide range of concentrations is not available in the literature, but there have been extensive studies of the pure components by X-ray crystallography, small angle neutron scattering (SANS) and NMR spectroscopy in bilayers, and of binary and ternary mixtures in monolayers as a function of surface pressure by the Langmuir–Blodgett (LB) technique. From these data, we estimated the molecular areas of DOPC and SM in the presence of Chol as summarised in Table 1. We chose values from the mixed monolayer studies at surface pressures that gave the same area/molecule as found in direct measurements of pure bilayers. This surface pressure was invariably close to the collapse pressure of the monolayer under study, and therefore its most condensed value. Although these variations of molecular area as a function of composition are estimates, the iterative procedure used to generate phase diagrams must produce a self-consistent result for all the compositions studied: self consistency could only be achieved by correcting for the surface area using the values in Table 1, indicating that they are reliable estimates.

There is some uncertainty in the value of r_{12}: since the precise position of the phase boundary is not known, we cannot calculate the average surface area per lipid in each phase. However, from our rough first estimation of the phase boundaries, we

Table 1 Estimated surface area per molecule of the pure lipids and binary mixtures used in the derivation of the phase diagram in Fig. 4, which takes into account the condensing effect of cholesterol. Values were available for hydrated bilayers or estimated from Langmuir–Blodgett studies of monolayers. Studies were performed at room temperature. For our analysis, we assumed linear expansion upon heating; therefore, there were no overall effect on the area ratios. This may be incorrect and, if so, would skew the position of the phase boundaries. However, in Fig. 4, our tie-line boundary compositions (circles) seem to agree with the fewer boundary positions determined when the phase boundary moves across the mean composition (red stars), indicating it might not be a problem in the relatively small range of temperature studied

Lipid(s)	Estimated mean surface area per molecule / Å^2	Source reference
DOPC	72.5	Nagle,[24] Liu[25]
SM (C16 : 0)	41	Maulik and Shipley,[26] Schmidt[23]
Chol	36	Mintzer,[27] Shieh,[28] Small,[29]
DOPC/Chol	$72.5 + \frac{52 - 72.5}{0.5}x, \quad x \in [0, 0.5]$ $52.5 + \frac{36 - 52}{0.2}(x - 0.5), \quad x \in [0.5, 0.7]$ $36, \quad x > 0.7$ where x is the mole fraction of cholesterol. 72.5 Å^2 at 100 mol% DOPC condensing linearly to 52 Å^2 at 50 mol% Chol then to 36 Å^2 at 70 mol% Chol, constant at 36 Å^2 between 70–100% Chol.	Ghandhavadi,[30] Mintzner[27]
SM/Chol	$41 + \frac{40 - 41}{0.1}x, \quad x \in [0, 0.1]$ $40, \quad x \in [0.1, 0.25]$ $40 + \frac{38 - 40}{0.15}(x - 0.25), \quad x \in [0.25, 0.4]$ $38 + \frac{44 - 38}{0.1}(x - 0.4), \quad x \in [0.4, 0.5]$ $44 \quad x > 0.5$ where x is the mole fraction of cholesterol. 41 Å^2 at 100 mol% SM condensing to 40 Å^2 at 10 mol% Chol, condensing to 38 Å^2 between 25–40% Chol, rising to 44 Å^2 at ≥50% mol.	Radhakrishnan,[31] Yuan,[21] Sun,[32] Chiu,[33] Smaby[34]
DOPC/SM	$72.5 + (51 - 72.5)x$, $x \in [0,1.0]$, where x is the mole fraction of SM. A very small condensing effect of SM on DOPC (approximately 20 times less than Chol); therefore, assume ideal mixing with a linear decrease from 72.5 Å^2 at 100% DOPC to 41 Å^2 at 100% SM.	van Duyl,[22] Yuan[21]

can estimate this value to a reasonable degree. In a phase separated region, the main quantitative information we have is the relative distance from the starting composition to each phase boundary along the straight tie line. For example, in the 63.75 mol % DOPC: 21.25% SM: 15.0% Chol mixture (Fig. 1), the AFM data indicates that the sample is 12.7% L_o phase and 87.3% L_d, which gives a tie-line ratio of 0.239 (0.239 being the relative distance to the L_d phase boundary and 1 being the relative distance

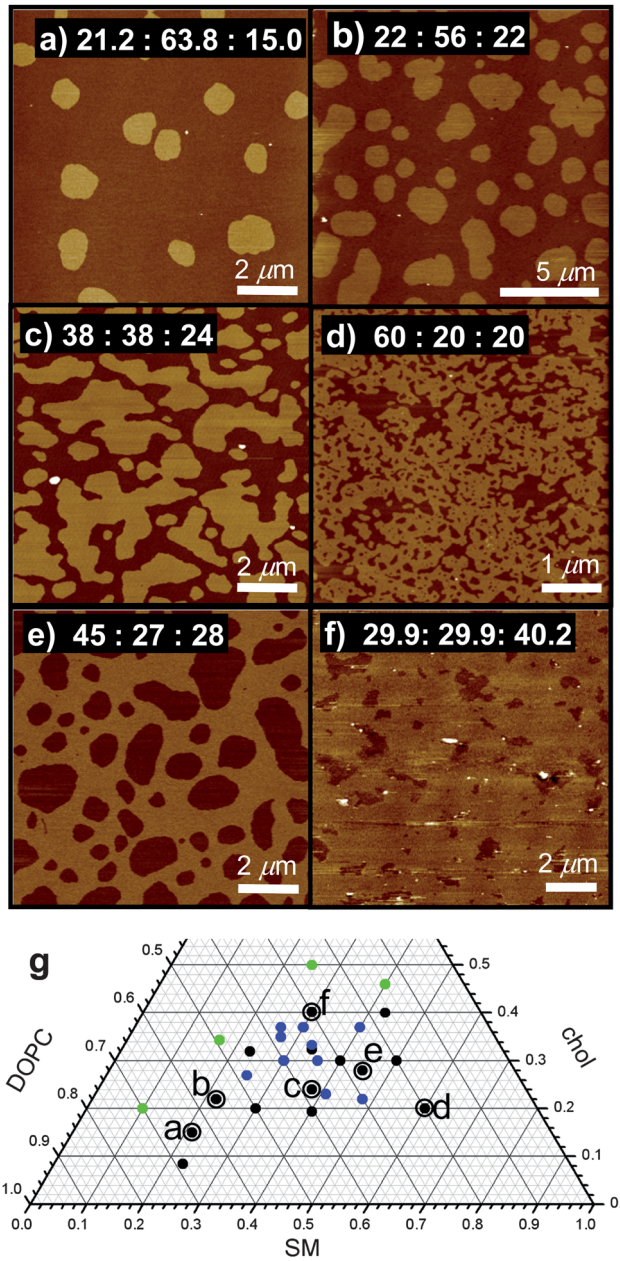

Fig. 1 A selection of AFM images of the SM : DOPC : Chol ternary model mixture, with compositions within the two-phase L_d–L_o region. All z-scales are 4 nm. Phase separation results in a wide range of morphologies, ranging from sparse isolated domains of L_o phase (a and b), through more continuous spinodal like structures (c and d), to the predominant L_o phase with a small quantity of the L_d phase (e and f). g is a ternary graph locating all the compositions studied. Black indicates the compositions studied only at 22.0 °C to accurately locate the phase boundary at room temperature; blue are around the critical region with full temperature ramps (see Fig. 2); and green are the single phases at 22.0 °C (images not shown).

to the L_o phase boundary). However, these are not absolute distances, so cannot be used in isolation to locate the exact orientation or length of the tie lines. Several thermodynamic rules and assumptions aid in finding the position of the two-phase boundary: a) tie-lines can never cross one another, b) the orientation of tie-lines close to one another will not vary greatly, c) a composition must lie within the bounds of the ternary phase diagram, and d) the two-phase boundary is relatively smooth and has no discontinuities. The temperature at which each composition crosses a boundary gives single precise locations in the temperature-phase space (marked with stars in the phase plots in Fig. 4), from which a rough indication of the position of the boundary can be plotted, together with an estimation of its progress with temperature. The final and crucial information for determining the tie line endpoints is the measurement of the height difference between the two phases. This measurement is analogous to the quadrupole splitting spectra measured by Veatch *et al.*[4] in their NMR measurements of deuterium labelled lipid bilayers. The further around the boundary one travels in each direction away from the critical point, the greater the height difference. Of particular importance is the fact that two compositions, which lie along the same tie line, will have domains with an identical composition (albeit at different area ratios according to the lever rule), so they will have an identical L_d–L_o height difference. Observation of the critical point behaviour gives the location of the critical point to within 5% for the four particular compositions studied. Tie-lines will converge on this critical point. The L_d–L_o height difference is plotted in Fig. 3, in this case at a fixed mean (critical point) composition as temperature increases, and the tie-line shrinks to zero. When two compositions are found to lie on, or at least very close to, the same tie-line, *e.g.*, the starting compositions of 40.3 mol% DOPC: 40.3% SM 1: 19.4% Chol and 68.7 mol% DOPC: 22.9% SM, 8.4% Chol, the two ratios along the same tie-line results in simultaneous equations, which can only be satisfied with the boundary in one position and solved exactly.

Results and discussion

Construction of a ternary phase diagram at room temperature

We chose to study the DOPC, sphingomyelin (SM) and cholesterol (Chol) mixture as our model of a cell membrane. This system has been widely studied over the years, and is thought to be a good analogue of cell membranes. In particular, the heterogeneity of the naturally derived egg-SM introduces a controlled degree of lipid complexity to the model. As a first step, a scattergun approach to the phase diagram was taken, with 17 compositions chosen across the phase diagram and imaged at a room temperature of 22 °C only (see Fig. 1 for a selection). Several compositions were in the single phase region, labelled in green. Using the method described above, a basic region of two phase separations was plotted as a guide. The images show a large variation in structure, and are very similar to those imaged *via* the fluorescence microscopy of GUVs, although with the capability of distinguishing domains with diameters down to 10 nm. Domain sizes tend to be smaller than those observed in GUVs due to the supported nature of the membrane, the proximity of the surface acting as a drag force on the diffusion of domains and hence slowing coalescence into the larger domains. Ostwald ripening does occur, just at a much slower rate (data not shown).

One interesting feature is the tilt of the tie-lines up towards the right hand side. All lipid species, including cholesterol, have the same diffusion coefficient within a single phase or domain. In other words, the diffusion is phase and not lipid molecule dependent. The driving force for lipid separation into L_d and L_o phases is the increasing difficulty for low T_m lipids to be incorporated into the highly ordered phase. Although some studies indicate that cholesterol partitions roughly equally into both phases, which would indicate that there is no specific interaction between the high T_m lipid and cholesterol, in this case the tilt of the tie-line up to the right

hand side of the ternary diagram would indicate that there is indeed a specific SM–chol interaction. This result has also been found in the work of Veatch.[10] This could be ascribed to a specific hydrogen bonding network[19] or the complexation of SM with cholesterol.[35]

Critical region

In order to locate the precise position of the critical point, and to track how it moves with temperature, a new scatter of compositions was prepared across a narrower range within the interior of the previously measured two-phase region, with a particular concentration around the estimated critical region. These are numbered 1–8 in Table 2, and marked in blue in Fig. 1 and 2. This time, imaging of the bilayer morphology was performed as a function of temperature, with increments of 0.5 °C in both the heating and cooling directions. The temperature was increased until all trace of the domain structure had disappeared. Fig. 2 shows a typical selection of images of various compositions selected to highlight the general trends, with the samples 5, 6, 1 and 7 (in that order) as a linear transect across the critical region from left to right. Samples 5 and 6 are clearly to the left of the critical point, with isolated domains of L_o surrounded by the L_d phase. Sample 5 is closer to the phase boundary, with the L_o phase disappearing 2 degrees before those in sample 6. It is interesting to note the non-circular domain boundary in comparison to the rounder domains in Fig. 1, which derive from compositions far to the left of the critical region. Even though here we are very much crossing a first order transition boundary, the line tension in the domains is considerably reduced. It should be possible to analyse these images in terms of the domain shape factor to derive a line tension, but we have not yet verified this approach on AFM images of supported membrane. On the other side of the critical region, sample 7 exhibits a continuous L_o phase with small islands of L_d phase. As the temperature increases, these final L_d domains disappear as the phase boundary is crossed in a first order phase transition. Again, despite the reversal in proportion, the domain boundaries are convoluted with low line tension in comparison with the more continuous L_o phase image in Fig. 1. Sample 1 in the middle of the transect is close to the critical point. At 24.0 °C the domains are approximately 50 : 50 L_d–L_o, and quite convoluted in nature. Around 26 °C, the domain edges suddenly roughen and break up, but do not disappear. Here, we are at, or very close to, a critical point. The pre-existing domain structure breaks down and is replaced by a more uniform spread of small domains. As the temperature increases (at considerably higher temperatures than the surrounding first order phase boundary), these small domains persist, although

Table 2 Compositions (molar ratios) studied around the critical region (numbers) and along the line of critical points (letters), which is accessed by changing the temperature

Label	Mol% SM	Mol% DOPC	Mol% Chol
1	33.3	33.3	33.3
2	30	33	37
3	26	37	37
4	23	45	32
5	25	48	27
6	30	40	30
7	40	23	37
8	40	30	30
A	27	38	35
B	36	34	30
C	41	36	23
D	48	30	22

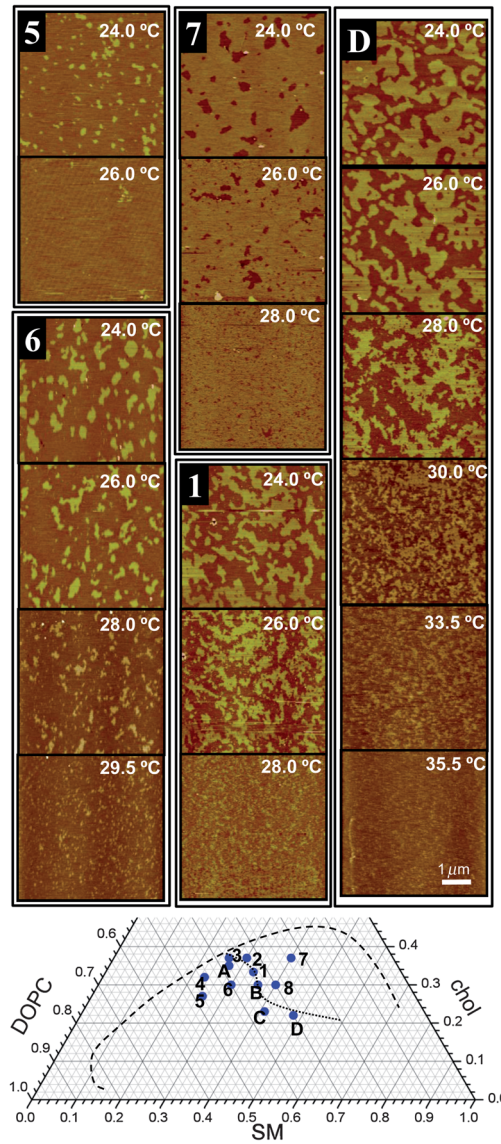

Fig. 2 Compositions focusing on the critical region. Numbers 1–8 indicate a sweep across the region, while A–D indicate a subsequent track along the estimated line of the critical points. To the left of the critical line (compositions 5 and 6 shown) L_o domains extinguish into the surrounding L_d phase with increasing T. To the right (composition 7), the minority L_d phase is gradually extinguished until a single L_o phase remains. On, or close to, the critical line (1 and D), rather than undergoing a simple first order phase transition, the domains gradually roughen below T_c, then suddenly break up into many very small compositional fluctuations, which persist for 5 or 6 degrees above T_c. The correlation length for these fluctuations diminishes as the temperature rises. Guide lines from Fig. 4, the dashed line is the L_d–L_o boundary at 24.0 °C and the dotted line is the estimated line of critical points as T increases. Samples 1, 2, 3, A, B and D exhibit critical like behaviour.

getting smaller and smaller, until they disappear around 34 °C. It is interesting to note that sample 1 is the 1 : 1 : 1 equimolar mixture, which is the composition most widely studied as a model of cell membranes. These small nanodomains are present to the same extent during both heating and cooling.

Following the identification of the critical point location, a further four compositions denoted A–D were produced to track down into the two-phase region toward the SM vertex, and track the motion of the line of critical points as the temperature is increased. Images from sample D are also shown in Fig. 2. Sample D has the longest run of pre-critical images simply due to it being the critical composition furthest from the room temperature phase boundary. The images produced are very similar indeed to those of sample 1, just at higher temperatures. Each of the compositions A–D showed behaviour indicative of a critical point at some point in the temperature ramp. It is unlikely that each of these compositions lie exactly on the critical point line (the non 50 : 50 molar ratio of phases below T_c being one indicator), so we must infer that the critical behaviour extends a short compositional distance from the exact line of critical points.

Using the ratios of the two observed phases from all of the temperature ramp data, together with the exact known boundary positions as each composition crosses into the single phase region and the difference in heights between the L_o and L_d phases (as described in the methods, Fig. 3), we plot the two-phase region as a function of temperature (Fig. 4). Although temperature increments of 0.5 °C were recorded, full analysis was only performed at the temperatures shown due to time constraints. We have been working on a computer algorithm that would use our construction rules to automatically generate a phase diagram from the image data. The individual plots were then combined to produce a map revealing the retreat of the two-phase region towards the lower right hand SM vertex as the temperature increases. The dashed line in this figure indicates the line of critical points. In Fig. 4, it can be seen that the end point of each tie-line (filled circles, which give the composition of each phase separated domain) do not always meet the indicated boundary. This is most likely a data collection *vs.* time problem. When acquiring AFM images at a fixed temperature it is possible to acquire more than 10 images in random locations on the sample in a reasonable amount of time, hence the large amount of sampling carried out at room temperature. However, when performing a temperature ramp with 0.5 °C increments from 24 to 45 °C, there are 42 steps and the maximum number of image areas that can be sampled at each temperature is perhaps 2 or 3 if one wishes to complete a single temperature ramp in a day. For this reason, several of the ramps had low sampling, below the ideal

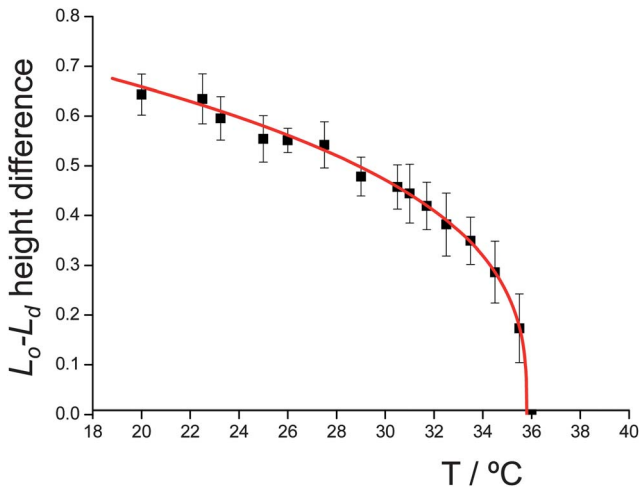

Fig. 3 The height difference between the L_o and L_d phases approaching a critical point. The fit is $0.262(T - 35.8)0.334$.

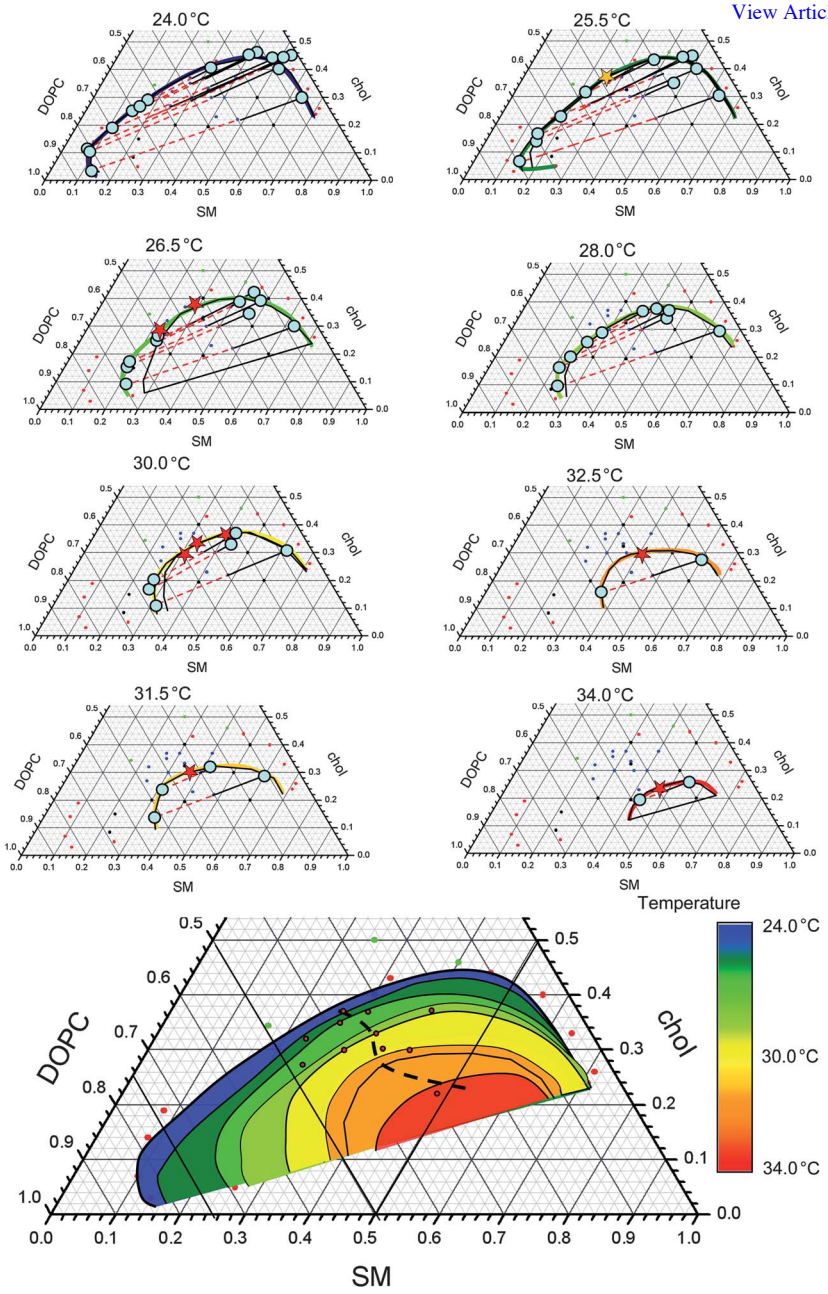

Fig. 4 (Top) Plots illustrating the calculation of boundary of the L_o–L_d two-phase co-existence region as a function of T, using the area information derived from the AFM images (using the lever rule together with a correction to account for the change in area per lipid molecule across the phase diagram), the tie-line slope is indicated by the height difference in the L_o and L_d phases and definite boundary markers, where the boundary crosses each composition and the final domain structures are extinguished (for a first order transition). These positions are marked with a red star and a gold star is used to indicate the precise critical point found. A filled circle marks the composition at the end of each tie-line. (Bottom) An amalgamation of the above individual plots, together with an estimation of the line of critical points measured in this study.

required to achieve confidence in each individual tie-line. However, in aggregate, all of the measured values plotted give a good indication of the boundary location.

Critical phenomena

The AFM images reveal critical phenomena in some detail. Fig. 5 is a highlight of the temperature ramp of sample D from just above T_c to nearly 10 °C higher. The images shown have been fully levelled then converted to a binary format to facilitate later automated image analysis. What appear to be small nanoscale domains are visible for $T \gg T_c$ and they diminish in size with increasing T. These are believed to be critical point fluctuations. Although it takes around 1.5 min to record each of these scans, at a maximum line scan rate of 5 Hz, the speed indicates that 5 lines will be recorded each second. As long as the correlation length (the characteristic length scale of the image features) is small enough, the image will represent a true picture of the length scale of the fluctuations, but cannot capture the frequency of fluctuation if this is less than approximately 5 s (using a repeated scan over a small region: a high aspect ratio scan). These fluctuating domains are classic signals of critical point behaviour and have not been imaged before with nanometre resolution.

Fig. 6 is another detail of sample D, this time highlighting the fluctuations in the domain boundary as T_c is approached from below, with the line tension falling to zero at T_c. The edges of the domain become ever more convoluted until just above T_c, where the domain structure suddenly breaks down into critical fluctuations with a length scale smaller than the pre-existing domains. As the temperature steps here were 0.5 °C it is unlikely that the exact critical point, where fluctuation at all length scales would be expected, was found.

Characterisation of critical fluctuations

The correlation function, or autocorrelation, is a measure of the probability of finding a similar structure (or fluctuation) as a function of distance. An excellent description of this may be found in the review by Honerkamp-Smith *et al.*[11] A correlation of 1 will indicate full correlation, 0 means random or no correlation, and −1 would be an anti-correlation. The correlation length, ξ, calculated from the correlation function, characterises the typical size of fluctuations as the temperature approaches T_c from a higher T. The order parameter we are measuring is the density of the bilayer. As these fluctuations are random within the plane of the bilayer, a

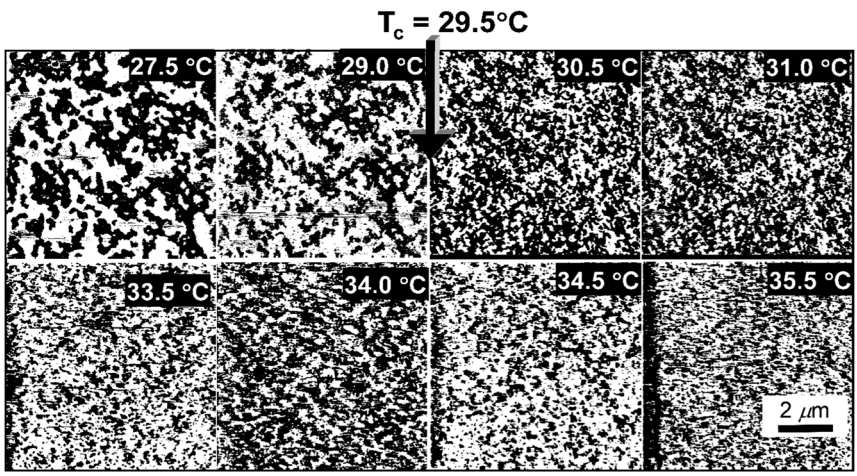

Fig. 5 Composition fluctuations in sample D as the temperature is increased above the critical point.

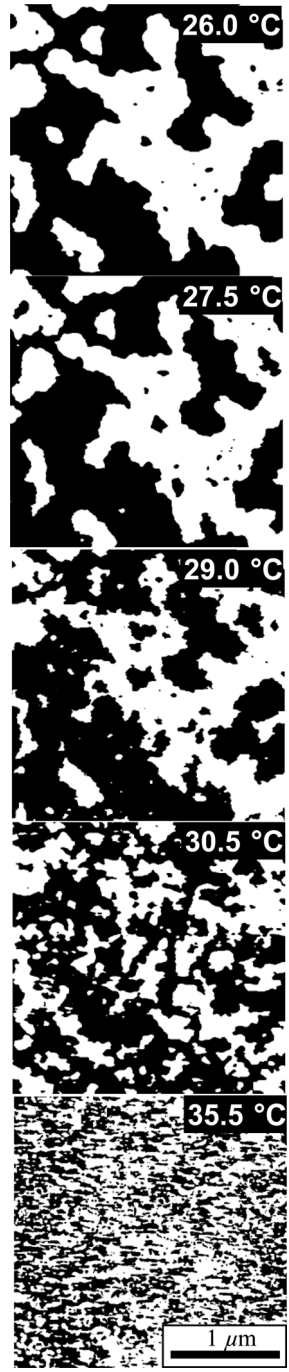

Fig. 6 Detail of sample D, highlighting a reduction in line tension approaching T_c. As the temperature increases towards $T_c = 29.5$ °C, the domain edges progressively roughen as the domain line tension reduces towards zero at T_c. Above T_c, the correlation length of the composition fluctuations reduces until, at $T \gg T_c$, the bilayer appears to be a single fluid phase. Images are 2.5 μm, digital zooms of 10 μm scans, and have been thresholded and converted to binary form to aid image analysis.

radially averaged correlation function can be used. This function was run as a Macro in Image J (NIH)[36] and used to analyse each image in the sequence once they that had been carefully levelled and converted into a binary format (again with Image J).

Fig. 7 shows a plot of the correlation functions for the image sequence of sample 1 starting just above T_c. The correlation functions fit exponential decays, whose decay length is characteristic of the correlation length. It can be clearly seen that the correlation length drops monotonically with an increase in T above T_c. At a $(T - T_c)$ of 0.7 °C the correlation length was 60 nm, dropping to 11 nm at $(T - T_c) = 5.25$ °C, reflecting the existence of a smaller correlation between the fluctuating domains. The model by which this critical behaviour may be understood depends upon its universality class. Any system that belongs to the same class should exhibit the same critical behaviour and scale the same way with temperature whether it is the spin in ferromagnets or liquid crystal orientations. For instance, the correlation length should always become very large as T_c is approached. This is given by $\xi = \xi_0|(T - T_c)/T_c|^{-\nu}$, where the term in the outer brackets is the reduced temperature (T_R) in Kelvin and ν is the critical exponent, which has a value particular to the model. This power law exponent is universal, but the value of ξ_0 depends upon the system

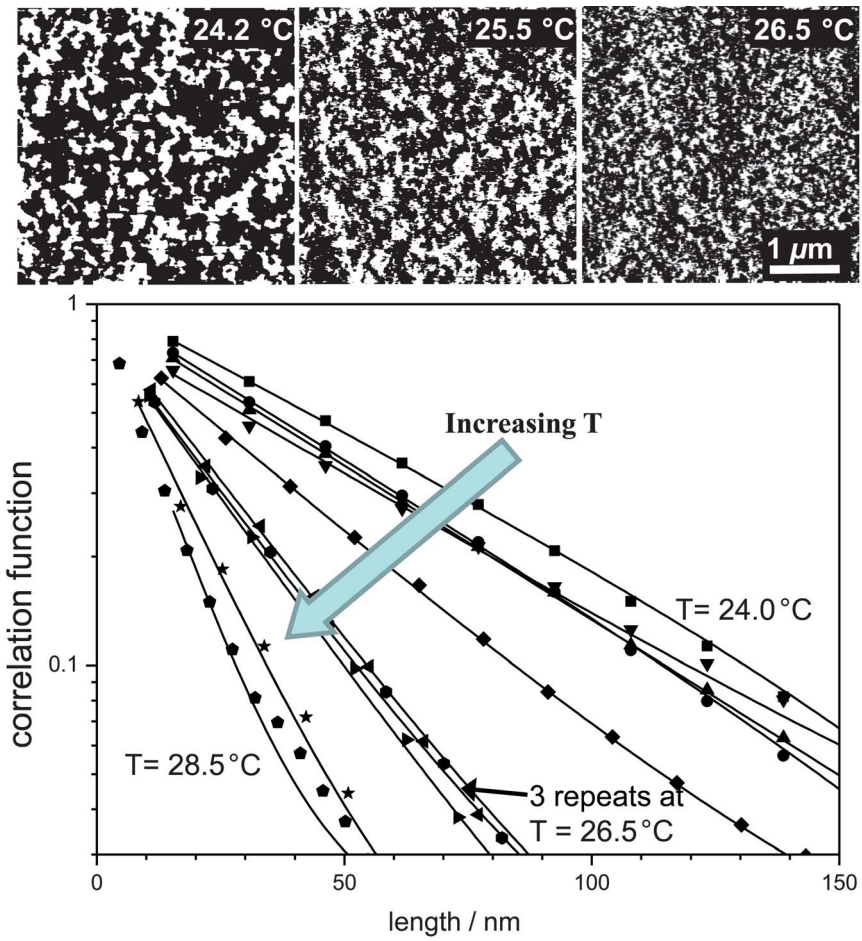

Fig. 7 Semi-log plot of the radially averaged correlation function of aample 1 just above T_c (23.25 °C), showing a reduction in the correlation length as the temperature increases. The images are a selection to illustrate the structures observed.

and should be related to the size of the smallest natural length (*e.g.*, a molecular size). As the correlation function should diverge as T asymptotically approaches T_c, we must obtain a more accurate measurement of T_c than that just obtained from looking at the images. Plotting the inverse of the correlation length against temperature (Fig. 8, top) gives a straight line which, when extrapolated to the x axis (and hence $\xi = \infty$), gives T_c. In this case, the actual T_c was 0.75 degrees lower than the temperature estimated by looking at the images.

The plot of $\log \xi$ against $\log T_R$ is given in Fig. 8 (bottom) for only a single temperature ramp of one component (sample 1). Although the data follows a roughly straight line, its slope $-\nu$ is around 0.8. The value of ν should depend only upon the model. For the 2D Ising model, the static exponent ν should equal 1, for the 3D Ising model $\nu = 0.630$ and for mean field theory $\nu = 0.5$. Each of these predictions is plotted on the graph as a line along with the measured data points. The actual best fit value is somewhat lower than the expected value for the 2D Ising model, although this is the closest model. This indicates that sample 1 is best described by the 2D Ising model. The non-exact correspondence to the 2D Ising model may be due to fluid hydrodynamic effect on the domain formation kinetics and also that of the substrate. Recent work by Haataja[37–39] shows theoretically that large fluctuations in compositional domains will induce the flow of lipid components and domain structures, thereby inducing flow fields in the surrounding fluid. The water is not a passive structure, its motion interacts and couples with the membrane, changing its behaviour. However, from a theoretical viewpoint, these dynamics should not affect energetic properties, such as ν.

The fluctuating nanodomains observed at temperatures above T_c range in size from 100 nm (fractionally above T_c) down to around 10 nm (about 7 °C above T_c). This is a considerable temperature differential, and is equivalent to nanodomains existing in the apparently single phase region above the critical point in the 40–50 mol% range at room temperature. AFM imaging has also determined that critical behaviour extends a reasonable distance either side of the line of the critical point (Fig. 3). This would indicate that the nanodomain region is quite substantial is size, and would be a prime candidate for the transient and small, but definitely present, raft like structures in cell membranes, as determined by NMR and FRET measurements. Unfortunately, this work does not shed any light on the reason for the difference between type I and type II lipids.

The presence of a spinodal domain structure at particular compositions in the two-phase region can now also be explained. If the thermal history of the sample takes the composition through a critical region during cooling, then a spinodal structure will result. On supported membranes, this continuous percolating structure may be rather fine as the surface drag prevents domain coalescence into larger spinodal swirls. Away from this critical region, first order phase transitions occur and the mechanism will revert to a nucleation and growth mode, leading to isolated domains.

Critical behaviour in membrane at $T \leq T_c$

Fluid flow within the membrane (*i.e.*, non-diffusive movement of a large body of molecules on average) is required when a phase is changing rapidly, such as near a critical point. This effect may be seen in Fig. 9, showing sequential images around 2.5 min apart. Here, the domain boundaries move around at an ever increasing rate as the critical point is approached. The domains are characterised as having increasingly convoluted boundaries as the line tension reduces towards zero at the critical point and a decreasing height difference between the L_o and L_d phases, which here is at the minimum, but clearly detectable at 0.15 nm in the final image. The first detectable appearance of smaller scale critical fluctuations within each phase is seen at 24.2 °C, by which point it is becoming increasingly difficult to distinguish the L_o and L_d domains, and the bilayer surface seems to roughen in the z direction.

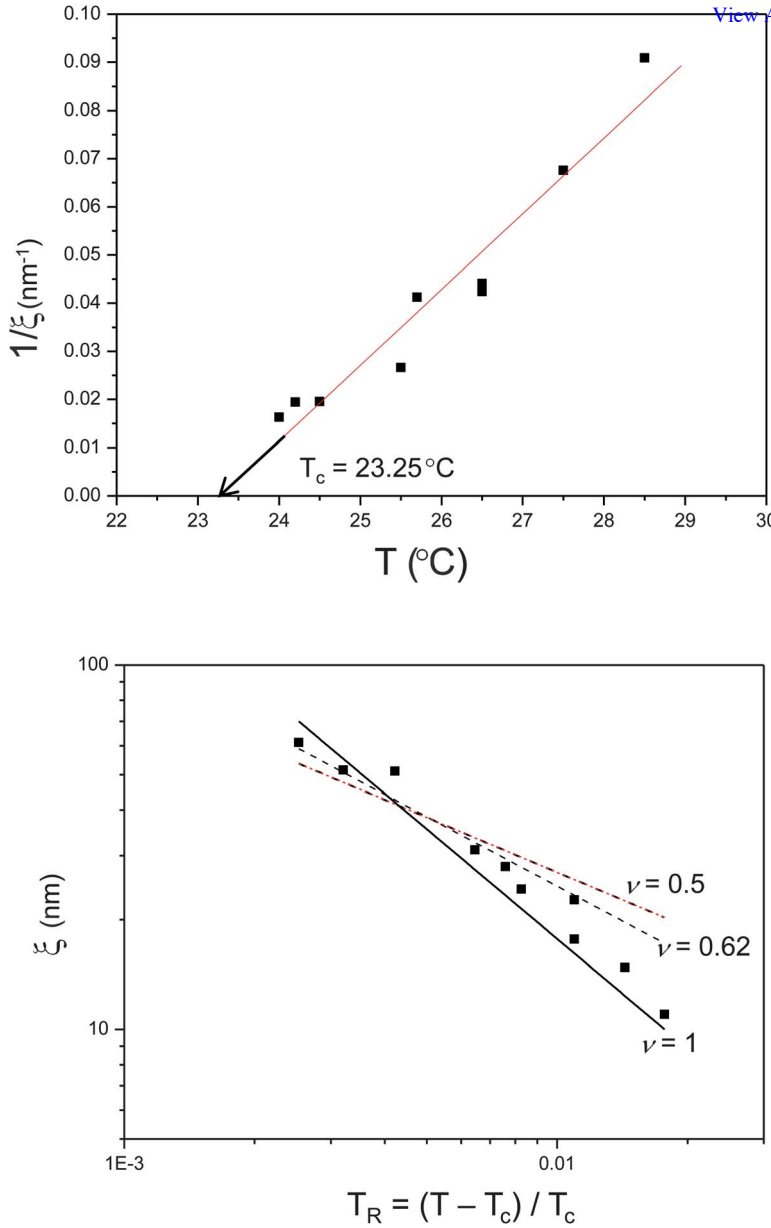

Fig. 8 (Top) The inverse of the correlation length ($1/\xi$) plotted against T for sample 1. The intercept gives the value of T_c, as verification of the experimentally observed T_c. (Bottom) Correlation length ξ plotted against the reduced temperature for one run of sample 1. The slope of the line gives the critical exponent $-\nu$. The solid black line shows the fit with $\nu = 1$, the dashed line shows $\nu = 0.62$ (3D Ising Model), and he dotted line gives $\nu = 0.5$ (mean-field theory). The best fit seems to be with $\nu = 1$, although the actual calculated best fit with equal weighting to all data points is in the vicinity of 0.8. These data verify that the transition we have observed in a solid supported bilayer is a critical transition.

Compare this with the smooth and clean bilayer surfaces seen in Fig. 1, which are stable L_o domains far from a critical point. The L_o domain, upon closer inspection, seems to be a mix of much smaller L_o and L_d domains. A zoom of this image is

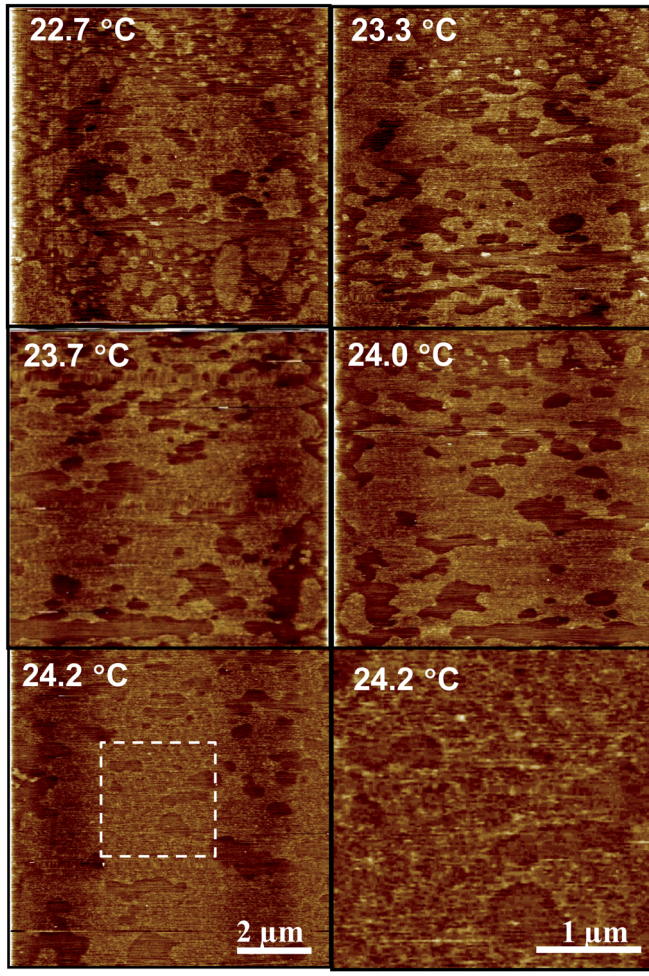

Fig. 9 Composition 3 (Fig. 2) approaching the critical point from below, where $T_c = 25.5$ °C. This critical region is marked as an gold star in Fig. 4. The normally stable domains (which have a low diffusion coefficient on a substrate) begin to undergo large scale changes about 3 degrees below the critical point, indicating flow fields within the membrane. The approach to criticality is also indicated by the smaller scale composition fluctuations within the apparently single phase domains, highlighted in the digital zoom of the 24.2 °C image (image z scale 1.5 nm).

provided in the final panel. Where the L_o and L_d domains below T_c have sizes from 100 nm to 1 μm, the fluctuations in the final image are characterised by a length scale of 50–80 nm (by observation rather than image analysis).

This dynamic behaviour is quite unusual in a surface supported membrane, where a viscous drag force from the surface slows down large scale domain motion. The diffusion of domain structures in GUVs has been modelled by Veatch and Cicuta.[40] Even though the diffusion coefficient of individual molecules within a membrane is only fractionally reduced by water or substrate interaction, the diffusion of domains is affected. For a domain of size r, the diffusion coefficient $D \sim 1/r$, reducing to $D \sim \ln(1/r)$ for small values of r. To our knowledge, no data exists for the diffusion on surfaces due to it being too slow. In 2006, Tserkovnyak *et al.*[41] showed theoretically that the diffusivity of a protein embedded in a supported membrane would take on a

strong power law dependence near a critical point, rather than the usual asymptotic behaviour. In other words, the local environment and proximity have far more of an influence on the membrane properties when near a critical point. What happens in this system at the exact critical point where fluctuations should be at all length scales? As the correlation length increases, the smaller fluctuations do not diminish. There are correlated regions at all length scales within measurable limits.

Fig. 10 shows sample 1, where the temperature has been increased from room temperature (22.0 °C) to 23.1 °C, just below the critical point ($T_c = 23.25$ °C) before the compositional fluctuations dominate and held stable for over an hour. These images are larger 10 μm scans and, as such, the smaller compositional fluctuations would not be visible at the 512×512 pixel resolution used (*i.e.*, unless they get to a size >100 nm, which should happen at T within 0.4 °C of the critical temperature). The images are also noisier due to the cooling systems required to maintain stable temperatures around room temperature (22–25 °C). Proximity to a critical point is confirmed by the low apparent surface tension and relatively rapid flow of the domains across the surface, coalescing into larger domains. 40 images in total were taken in this sequence and numbered sequentially (the number of each image in the sequence is shown in the top right of each panel), with each scan taking approximately 3 min. The striking feature of these images is the repeated reversal of image contrast, with the L_o and L_d phase swapping round in the space of a couple of scan lines (around 1 s). These events are indicated by a yellow star. In many years of imaging membranes using AFM in our laboratories, this effect has only ever been observed at a critical point. We attribute this to large density fluctuations on a scale bigger than the image size of 10 μm. However, the mechanism for the image reversal is unclear. AFM imaging only reports the difference in height between the two phases, not their absolute heights. One possibility is that the L_d and L_o phases are actually swapping around, with the L_d phase thickening and the L_o phase thinning, although this seems implausible as the rate of diffusion of molecules from one phase to another would have to be very fast. Another possibility is that, as the phase changes, molecules partially move out of the L_o phase (presumably the most mobile component would move), which then leads to a partial collapse

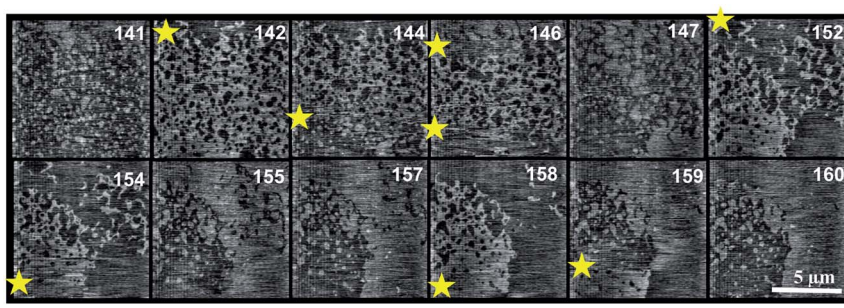

Fig. 10 Selected images from a time sequence of a single area of sample 1 (1.5 min per scan, images numbered sequentially), with the temperature maintained at $T = 23.1$ ($T_c = 23.25$ °C). As well as the dynamic motion of domain boundaries due to flow fields, low line tension indicated by the convoluted domain boundaries and obvious, but slow, Ostwald ripening, a striking feature in these images is the inversion of the contrast at the points marked with a yellow star. We have only rarely observed this behaviour when approaching a critical point from lower temperatures and the temperature is then held stable. We believe these to be composition fluctuations on a length scale larger than the image size (10 μm) where, due to the proximity of the surface, the lipid molecules cannot flow quickly enough across the surface. This leads to a partial collapse of one phase. This interpretation is provisional as, although the absolute bilayer depths can be easily measured *via* AFM force spectroscopy,[6] AFM imaging will only report the difference in height between the two phases if no defects are present as a reference. The image noise is due to the cooling system required to maintain T at or just below room temperature.

of the former L_o phase to a height lower than the L_d phase. We are currently devising experiments to investigate this further. However, we also note that the area change upon the changing height will provide an additional internal constraint. The domains interact with each other according to their proximity and they can flip to keep the total area unchanged (a "compressible Ising model").

Conclusion

In this paper, we have demonstrated that AFM can be an illuminating technique in the study of critical phenomena, obtaining results which are in some agreement with other recent work, but most importantly bridging the length scales from fluorescence microscopy of GUVs (low resolution) to the molecular scale measurements (NMR, FRET). In doing so, we have confirmed what many have long suspected: the existence of somewhat transient nanodomains within the high cholesterol single phase in the vicinity of a critical point. The phase separation is consistent with a critical phase transition that follows the 2D Ising model, in agreement with recent papers by Honerkamp-Smith and Veatch. In summary, compositional fluctuations were measured and characterised, with nanodomains 10–100 nm in diameter existing at temperatures up to 7 °C higher than T_c. At room temperature, this is equivalent to nanodomains existing in the 40–50% Chol region above the critical point, and extending 10% either side of the lipid composition of the critical point. The temperatures where these structures were found ranged from 24 °C to nearly 40 °C (dependant upon composition), clearly in the biological range. As this simple model system has been found to have a phase diagram nearly identical to that of biologically derived plasma membranes,[42] this finding must have important implications to the study of lipid rafts in real cell membranes.

References

1 G. W. Feigenson, *Biochim. Biophys. Acta, Biomembr.*, 2009, **1788**, 47.
2 S. L. Veatch, I. V. Polozov, K. Gawrisch and S. L. Keller, *Biophys. J.*, 2004, **86**, 2910.
3 T. Salditt, *J. Phys.: Condens. Matter*, 2005, **17**, R287.
4 S. L. Veatch, K. Gawrisch and S. L. Keller, *Biophys. J.*, 2006, **90**, 4428.
5 R. R. M. de Almeida, L. M. S. Loura, A. Fedorov and M. Prieto, *J. Mol. Biol.*, 2005, **346**, 1109.
6 M. C. Giocondi, V. Vie, E. Lesniewska, P. E. Milhiet, M. Zinke-Allmang and C. Le Grimellec, *Langmuir*, 2001, **17**, 1653.
7 C. D. Blanchette, W.-C. Lin, C. A. Orme, T. V. Ratto and M. L. Longo, *Biophys. J.*, 2008, **94**, 2691–2697.
8 B. B. Machta, S. Papanikolaou, J. P. Sethna and S. L. Veatch, *Biophys. J.*, 2011, **100**, 1668.
9 S. Doniach, *J. Chem. Phys.*, 1978, **68**, 4912.
10 S. L. Veatch, O. Soubias, S. L. Keller, K. Gawrisch, Proc. Natl. Acad. Sci. U. S. A., **104**, 17650.
11 A. R. Honerkamp-Smith, S. L. Veatch and S. L. Keller, *Biochim. Biophys. Acta, Biomembr.*, 2009, **1788**, 53.
12 A. R. Honerkamp-Smith, P. Cicuta, M. D. Collins, S. L. Veatch, M. Den Nijs, M. Schick and S. L. Keller, *Biophys. J.*, 2008, **95**, 236.
13 P.-F. Lenne and A. Nicolas, *Soft Matter*, 2009, **5**, 2841.
14 M. L. Fanani and B. Maggio, *J. Phys. Chem. B*, 2011, **115**, 41.
15 S. L. Veatch and S. L. Keller, *Biophys. J.*, 2003, **85**, 3074.
16 S. A. Johnson, B. M. Stinson, M. Go, L. M. Carmona, J. I. Reminick, X. Fang and T. Baumgart, *Biochim. Biophys. Acta, Biomembr.*, 2010, **1798**, 1427.
17 E. L. Goksu, J. M. Vanegas, C. D. Blanchette, W.-C. Line and M. L. Longo, *Biochim. Biophys. Acta, Biomembr.*, 2009, **1788**, 254.
18 B. Seantier, C. Breffa, O. Félix and G. Decher, *Nano Lett.*, 2004, **4**, 5.
19 C. Das, K. Sheikh, P. D. Olmsted and S. D. Connell, *Phys. Rev. E: Stat., Nonlinear, Soft Matter Phys.*, 2010, **82**, 041920.
20 J. Juhasz, F. J. Sharom and J. H. Davis, *Biochim. Biophys. Acta, Biomembr.*, 2009, **1788**, 2541.
21 C. B. Yuan, J. Furlong, P. Burgos and L. J. Johnston, *Biophys. J.*, 2002, **82**, 2526.

22 B. Y. Van Duyl, D. Ganchev, V. Chupin, B. de Kruijff and J. A. Killian, *FEBS Lett.*, 2003, **547**, 101.
23 C. F. Schmidtt, Y. Barenholz and T. E. Thompson, *Biochemistry*, 1977, **16**, 2649.
24 J. F. Nagle and S. Tristram-Nagle, *Biochim. Biophys. Acta, Rev. Biomembr.*, 2000, **1469**, 159.
25 Y. Liu, PhD Thesis, 2003, Carnegie Mellon University, available at: http://lipid.phys.cmu.edu.
26 P. R. Maulik and G. G. Shipley, *Biochemistry*, 1996, **35**, 8025.
27 E. A. Mintzer, B.-L. Waarts, J. Wilschutt and R. Bittman, *FEBS Lett.*, 2002, **510**, 181.
28 H.-S. Shieh, L. G. Hoard and C. E. Nordman, *Acta. Cryst.*, 1981, **B37**, 1538.
29 D. M. Small, Sterols and sterol esters in *The Physical Chemistry of Lipids* 1986, Plenum press, New York, 40.
30 M. Ghandhavadi, D. Allende, A. Vidal, S. A. Simon and T. J. McIntosh, *Biophys. J.*, 2002, **82**, 1469.
31 A. Radhakrishnan and H. M. McConnell, *Proc. Natl. Acad. Sci. U. S. A.*, 2002, **99**, 13391.
32 W.-J. Sun, R. M. Suter, M. A. Knewston, C. R. Worthington, S. Tristram-Nagle and R. Zhang, *Phys. Rev. E: Stat. Phys., Plasmas, Fluids, Relat. Interdiscip. Top.*, 1994, **49**, 4665.
33 S. W. Chiu, S. Vasudevan, E. Jakobsson, R. J. Mashl and H. Larry-Scott, *Biophys. J.*, 2003, **85**, 3624.
34 J. M. Smaby, M. Momsen, V. S. Kulkarni and R. E. Brown, *Biochemistry*, 1996, **35**, 5696.
35 A. Radhakrishnan and H. M. McConnell, *Biophys. J.*, 1999, **77**, 1507.
36 Radially Averaged Autocorrelation Function Macro for ImageJ, Michael Schmid, 27-9-2011 update.
37 M. Haataja, *Phys. Rev. E: Stat., Nonlinear, Soft Matter Phys.*, 2009, **80**, 020902.
38 J. Fan, T. Han and M. Haataja, *J. Chem. Phys.*, 2010, **133**, 235101.
39 T. Han and M. Haataja, *Phys. Rev. E: Stat., Nonlinear, Soft Matter Phys.*, 2011, **84**, 051903.
40 S. L. Veatch, P. Cicuta, P. Sengupta, A. Honerkamp-Smith, D. Holowka and B. Baird, *ACS Chem. Biol.*, 2008, **3**, 287.
41 Y. Tserkovnyak and D. R. Nelson, *Proc. Natl. Acad. Sci. U. S. A.*, 2006, **103**, 15002.
42 S. L. Veatch, O. Soubias, S. L. Keller and K. Gawrisch, *Proc. Natl. Acad. Sci. U. S. A.*, 2007, **104**, 17650.